AFRL-RH-FS-TR-2022-0020

Applicability of a Dielectrophoresis-Based System For Viral Incapacitation

Caden B. Deverter
Claire Y. Li
SAIC, Inc.

Andrew W. Wharmby
711th Human Performance Wing
Airman Systems Directorate
Bioeffects Division
Optical Radiation Bioeffects Branch

12 August 2022

Interim Report - June 2022 - August 2022

Air Force Research Laboratory
711th Human Performance Wing
Airman Systems Directorate
Bioeffects Division
Optical Radiation Bioeffects Branch
JBSA Fort Sam Houston, Texas 78234

NOTICE AND SIGNATURE PAGE

Using Government drawings, specifications, or other data included in this document for any purpose other than Government procurement does not in any way obligate the U.S. Government. The fact that the Government formulated or supplied the drawings, specifications, or other data does not license the holder or any other person or corporation; or convey any rights or permission to manufacture, use, or sell any patented invention that may relate to them.

This report was cleared for public release by the AFRL Public Affairs Office and is available to the general public, including foreign nationals. Copies may be obtained from the Defense Technical Information Center (DTIC) (http://www.dtic.mil).

"Applicability of a Dielectrophoresis-Based System For Viral Incapacitation"

(AFRL-RH-FS-TR- 2022 0020) has been reviewed and is approved for publication in accordance with assigned distribution statement.

FERRIS.LYNDSEY.MARIE.1381070391 Digitally signed by FERRIS.LYNDSEY.MARIE.1381070391 Date: 2022.08.25 16:47:48 -05'00'

LYNDSEY M. FERRIS, Maj, USAF, BSC
Chief, Optical Radiation Bioeffects Branch

MILLER.STEPHANIE.A.1230536283 Digitally signed by MILLER.STEPHANIE.A.1230536283 Date: 2023.04.02 15:42:33 -05'00'

STEPHANIE A. MILLER, DR-IV, DAF
Chief, Bioeffects Division
Airman Systems Directorate
711th Human Performance Wing
Air Force Research Laboratory

This report is published in the interest of scientific and technical information exchange, and its publication does not constitute an official position of the U.S. Government.

REPORT DOCUMENTATION PAGE

PLEASE DO NOT RETURN YOUR FORM TO THE ABOVE ORGANIZATION.

1. REPORT DATE	2. REPORT TYPE	3. DATES COVERED	
		START DATE	END DATE
12-AUG-2022	Interim Report	JUN 2022	AUG 2022

4. TITLE AND SUBTITLE

Applicability of a Dielectrophoresis-Based System For Viral Incapacitation

5a. CONTRACT NUMBER	5b. GRANT NUMBER	5c. PROGRAM ELEMENT NUMBER
FA8650-19-C-6024		
5d. PROJECT NUMBER	**5e. TASK NUMBER**	**5f. WORK UNIT NUMBER**
		H14B

6. AUTHOR(S)

Caden Deverter, Claire Li, Andrew Wharmby

7. PERFORMING ORGANIZATION NAME(S) AND ADDRESS(ES)

Air Force Research Laboratory
711th Human Performance Wing
Airman Systems Directorate
Bioeffects Division
Optical Radiation Bioeffects Branch
4141 Petroleum Dr
JBSA Fort Sam Houston TX, 78234

SAIC, Inc.
4141 Petroleum Dr
JBSA Fort Sam Houston TX, 78234

8. PERFORMING ORGANIZATION REPORT NUMBER

9. SPONSORING/MONITORING AGENCY NAME(S) AND ADDRESS(ES)	10. SPONSOR/MONITOR'S ACRONYM(S)	11. SPONSOR/MONITOR'S REPORT NUMBER(S)
Air Force Research Laboratory 711th Human Performance Wing Airman Systems Directorate Bioeffects Division Optical Radiation Bioeffects Branch	711 HPW/RHDO	AFRL-RH-FS-TR-2022-0020

12. DISTRIBUTION/AVAILABILITY STATEMENT

DISTRIBUTION STATEMENT A. Approved for public release; distribution is unlimited. Cleared: AFRL PA Case Number: AFRL-2023-1851. The views expressed are those of the author and do not necessarily reflect the official policy or position of the Department of the Air Force, the Department of Defense, or the United States Government.

13. SUPPLEMENTARY NOTES

note

14. ABSTRACT

The recent COVID-19 pandemic has revealed a growing demand for methods of incapacitating virions in an effective and non-invasive manner. A dielectrophoresis (DEP)-based approach that could result in a permanent deformation of the virion structure and thus compromise its function is proposed and tested. A method for characterizing dielectric parameters of cells, virions, and nanoparticles is also discussed. Preliminary results suggest that an electric field of large magnitude could be applied to alter the virion structure.

15. SUBJECT TERMS

Dielectrophoresis, surface plasmon resonance, extraordinary optical transmission, COVID-19, nanoparticles

16. SECURITY CLASSIFICATION OF:			17. LIMITATION OF ABSTRACT	18. NUMBER OF PAGES
a. REPORT	b. ABSTRACT	c. THIS PAGE		
U	U	U	U	42

19a. NAME OF RESPONSIBLE PERSON	19b. PHONE NUMBER *(include area code)*
Eric Beier	(210) 539-8503

This Page Intentionally Left Blank

TABLE OF CONTENTS

LIST OF FIGURES

LIST OF TABLES

LIST OF EQUATIONS

ACKNOWLEDGEMENTS

This study was made possible by Aimee Price and The Ohio State Nanomaterials West Lab, who supplied the gold nanohole arrays. The authors would also like to thank Gary Noojin and Capt. Derek Barbee for their insight.

1.0 ABSTRACT

The recent COVID-19 pandemic has revealed a growing demand for methods of incapacitating virions in an effective and non-invasive manner. A dielectrophoresis (DEP)-based approach that could result in a permanent deformation of the virion structure and thus compromise its function is proposed and tested. A method for characterizing dielectric parameters of cells, virions, and nanoparticles is also discussed. Preliminary results suggest that an electric field of large magnitude could be applied to alter the virion structure.

2.0 INTRODUCTION

Dielectrophoresis (DEP) is a phenomenon that occurs when polarizable dielectric particles are subject to an inhomogenous electric field. The electric field induces a dipole in these particles [1]. In a homogeneous electric field, there is an equal force on each end of the dipole when it is aligned with the electric field. As shown in Figure 1, when a dielectric particle is in an area of inhomogeneous electric field, there are unequal forces on each electric pole, leading to a net force. Thus, in a nonuniform electric field, a dielectric particle experiences forces toward areas of maximum or minimum field intensity depending on the alignment of its dipole. These forces are referred to as positive and negative DEP, respectively.

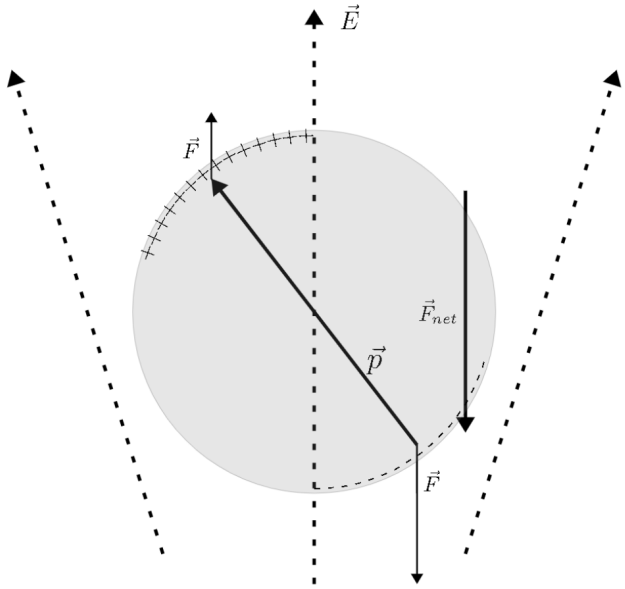

Figure 1. An unequal force on the ends of an induced dipole ($\vec{p}$) causes a net force ($\overrightarrow{F}$) to be applied to a spherical dielectric particle. In this case, the intrinsic charge relaxation processes of the particle and medium allow the dipole to have a component in the direction of the electric field vector, resulting in positive DEP. In negative DEP, the dipole is in opposition to the applied field, and the particle experiences negative DEP. The density of the electric field lines ($\overrightarrow{E}$) indicate field strength.

The DEP force depends on the relative permittivities and conductivities of the particle and its medium. Due to the frequency dependence of these terms, the sign of the DEP force is not constant, and is expressed in the Clausius-Mossotti function:

$$f_{CM} = \frac{\varepsilon_p^* - \varepsilon_m^*}{\varepsilon_p^* + 2\varepsilon_m^*}. \tag{1}$$

Equation 1. Clausius-Mossotti function

Here, ε_p^* and ε_m^* are the particle and medium's complex permittivity ($\varepsilon^* = \varepsilon' - i\frac{\sigma}{\omega}, i = \sqrt{-1}$) respectively, and σ_p and σ_m are the conductivity of the particle and medium respectively. The Clausius-Mossotti function is a function of the angular frequency of the incident electromagnetic field (ω), as complex permittivity and conductivity values vary with ω. The real portion of f_{CM} determines the component of the particle's dipole aligned with the external electric field and thus the sign of the dielectrophoretic force.

DEP has been used to manipulate, sort, and study structures ubiquitous in the biological world. DEP studies have also been used to study biological structures such as cells and virions, as these structures can be modeled as a layered dielectric sphere [1]–[3]. One characteristic of DEP not yet fully investigated is its effect on the viability of virions. The outbreak of the recent Coronavirus Infectious Disease 2019 (COVID-19) pandemic has resulted in a dramatic increase in demand for techniques to mitigate the spread of infectious diseases. DEP as a viral incapacitation method is a yet unexplored application of this previously well-studied phenomenon.

For this experiment, 100 nm diameter polystyrene (PS) nanospheres were selected as a model virus due their similarity in size and shape to the Severe Acute Respiratory Syndrome Coronavirus 2 (SARS-CoV-2). Analyzing the movement of the nanospheres under varying electric field frequencies reveals the material properties of the nanospheres; a change from the standard polystyrene permittivity value would mean that the spherical structure has in some way been altered. This experiment seeks to understand whether an electric field, when applied to a virus, can alter its structure and thereby compromise its function. The PS nanospheres used are believed to be more resistant to deformation than a virion, so a change in material properties for the nanospheres implies that under the same force, virion structure will also be modified. Knowing the changes that are possible in PS nanospheres establishes a foundation for the DEP technique to later be applied to viruses such as SARS-CoV-2.

3.0 BACKGROUND

The expression for the dielectrophoretic force on a homogeneous spherical dielectric particle is given by

$$\overrightarrow{F}_{DEP} = 2\pi R^3 \varepsilon_m Re[f_{CM}] \nabla E_{rms}^2 \tag{2}$$

Equation 2. Expression for the dielectrophoretic force

where R is the radius of the particle, ε_m is the permittivity of the medium, E_{rms} is the

root-mean-square electric field value, and f_{CM} is the Clausius-Mossotti function. The sign of $\overrightarrow{F}_{DEP}$ is determined by the sign of the Clausius-Mossotti function. More specifically, if the permittivity of the particle (ε_p) is greater than the permittivity of the medium (ε_m), then $f_{CM} > 0$ and the particle experiences positive DEP. Conversely, if $\varepsilon_m > \varepsilon_p$, then $f_{CM} < 0$ and the particle experiences negative DEP.

A dielectric particle in an electric field gradient does not experience solely translational effects. In particles that exhibit ohmic conduction or any number of relaxation processes, the dipole induced in the dielectric particle exhibits phase lag with respect to the field as shown in Figure 2. This is due to both dissipative processes and the finite time the particle takes to become polarized. This lag is quantified in the imaginary part of the f_{CM}.

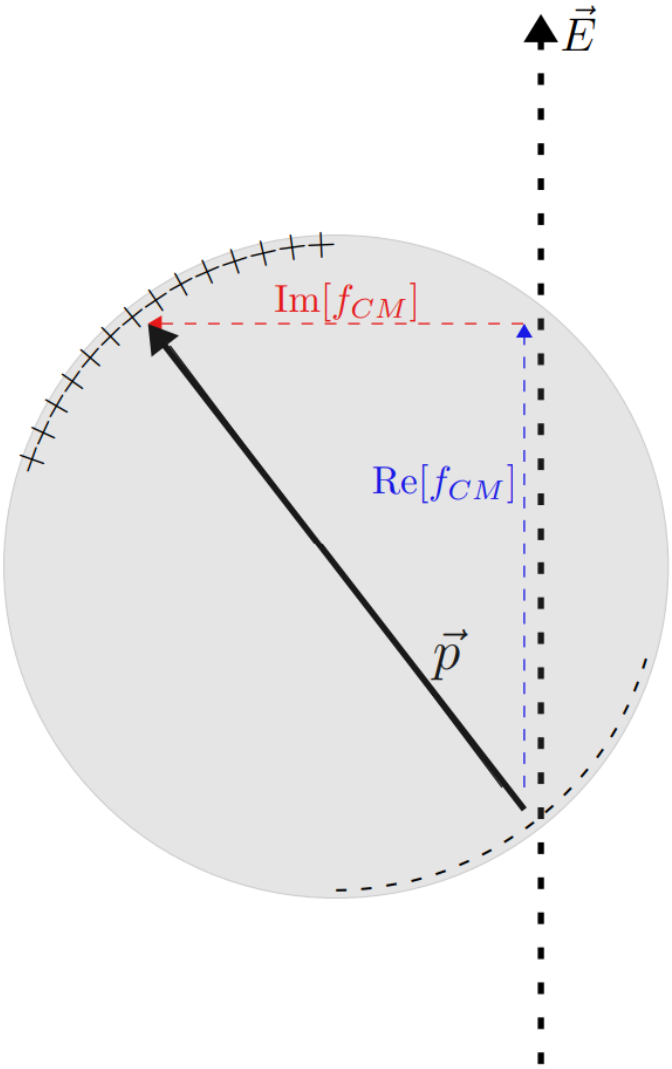

Figure 2. Phasor depiction of the lag between the induced dipole ($\vec{p}$) in a dielectric sphere and the electric field.

The phase lag of the dipole causes a torque to be applied on the particle by the electric field, which is given by [1]

$$\tau_{DEP} = -4\pi\varepsilon_m R^3 Im[f_{CM}]E^2. \tag{3}$$

Equation 3. Expression for dielectrophoretic torque

Here, $\mathrm{Im}[f_{CM}]$ is the imaginary part of the Clausius-Mossotti function and represents the component of the dipole perpendicular to the applied field. The frequency at which the $\mathrm{Im}[f_{CM}]$ is a minimum is that at which the greatest phase lag occurs due to a relative maximum of dissipative

processes. Knowledge of the Clausius-Mossoti function thus allows a detailed understanding of the forces and dissipative processes of a dielectric particle suspended in a medium.

The dependence of f_{CM} on the electrical properties of the system enables the determination of dielectric properties for many common particles [4]. For instance, the frequency where the Re[f_{CM}] = 0, termed the crossover frequency, can be related to the real permittivity of the particle and medium by [5]

$$\omega_c = \sqrt{\frac{(\sigma_m - \sigma_p)(\sigma_p + 2\sigma_m)}{(\varepsilon_p - \varepsilon_m)(\varepsilon_p + 2\varepsilon_m)}}. \tag{4}$$

Equation 4. Expression for the crossover freqeuncy of the DEP force

At the crossover frequency, the DEP force on the dielectric particles is zero and any change in a single dielectric property of the materials can be solved for by setting Equation 7 equal to zero, or, equivalently, by setting Equation 4 equal to the observed angular crossover frequency. Then, the properties from Equation 4 can be substituted into Equation 2 to calculate the force on the particle due to DEP. Analysis of the dielectrophoretic forces on water and polystyrene (PS) at sub-gigahertz ranges allows the unambiguous determination of the dielectric properties of the particle [6]–[8].

DEP can also accelerate the detection times of diffusion-based sensing methods. A technique published by Barik et al. [9] leverages DEP and alternating current (AC) electro-osmotic forces to trap analyte molecules on the surface of a gold nanohole array undergoing surface plasmon resonance (SPR). In SPR, electrons in the conduction band of a metal oscillate along the metal's surface as the metal refracts light. The energy of propagating SPR waves is dependent on the electric surroundings of the array and is thus highly sensitive to surface binding events. AC electro-osmosis refers to the fluid flow near electrodes due to the net tangential component of the electric field at the plate [10]. This force is exerted on charged species in solution, which then initiate bulk fluid flow due to viscous forces. In a nanohole array where a potential is applied, the greatest electric field gradient occurs at the edge of a nanohole. As the DEP force is directly proportional to the magnitude of the electric field gradient, the strongest DEP force is also experienced at the nanohole edge; this effect is shown in Figure 18. The DEP force thus works in concert with AC electro-osmosis to trap the nanospheres against the edge of the gold nanoholes [9]–[11].

When an analyte molecule is trapped on the surface of the array, the change of the refractive index at the metal-water interface causes the transmission spectrum to shift toward longer wavelengths [9]. This shift in wavelength is detected from light passing through the array due to the extraordinary optical transmission (EOT) effect. In EOT, light incident on a porous metallic surface with repeating topography passes through with unexpectedly high intensity due to constructive interference of localized surface plasmons [12]. The dielectric system described by Barik et. al. enables label-free detection of analyte molecules in fractions of the time typical for diffusion-based biosensors.

Previously, DEP has been used to study and manipulate particles across a broad frequency range, however, less work has been done to evaluate the effects of high voltages on particles undergoing DEP. Notably, the dielectrophoretic force is proportional to voltage (V) and a characteristic length of the electrode (L_c) by the expression [1]

$$\vec{F}_{DEP} \propto \frac{V^2}{L_c^3}. \tag{5}$$

Equation 5. Proportionality relation for the dielectrophoretic force

Thus, the efficiency of DEP-based systems may be maximized by both minimizing electrode dimensions and applying large voltages across the electrode gap. This work aims to evaluate the effects of high voltage DEP on PS nanospheres and experimentally validate previous work on a DEP-enhanced plasmonic sensor.

4.0 EXPERIMENTAL METHODS

A DEP-enhanced plasmonic sensor system was recreated based on Barik et. al. [9]. A diagram of the device is shown in Figure 3.

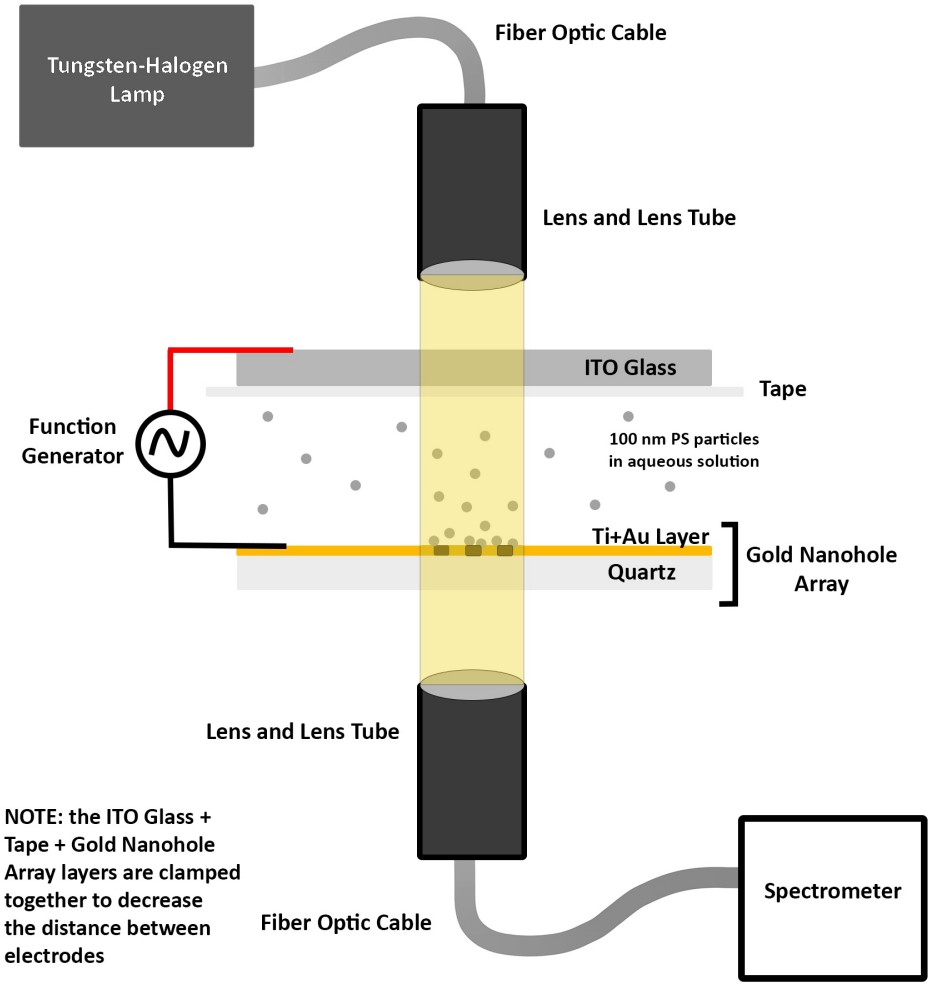

Figure 3. DEP experimental design. Note the ITO glass, tape, and gold nanohole array layers are clamped together to decrease the distance between electrodes.

The main sensor and plasmon substrate of the system is a periodic gold nanohole array. The array fabrication process is summarized in Figure 4. A 2 mm x 2 mm array of 160 nm holes spaced 600 nm center-to-center was fabricated by electron beam lithography and liftoff. First, a layer of photo/electron beam resist was spun onto a quartz substrate, patterned by electron beam lithography, then developed leaving an array of holes in the photoresist. Next, 10 nm of Ti and 90 nm of Au were deposited by electron beam evaporation onto the photoresist patterned quartz. Finally, the resist mask and excess metal adhered to the photoresist were removed by soaking and ultrasonic agitation in solvents, leaving the Ti/Au on the quartz with the 2 mm x 2 mm array of 160 nm holes. The resulting array structure is shown in Figure 5.

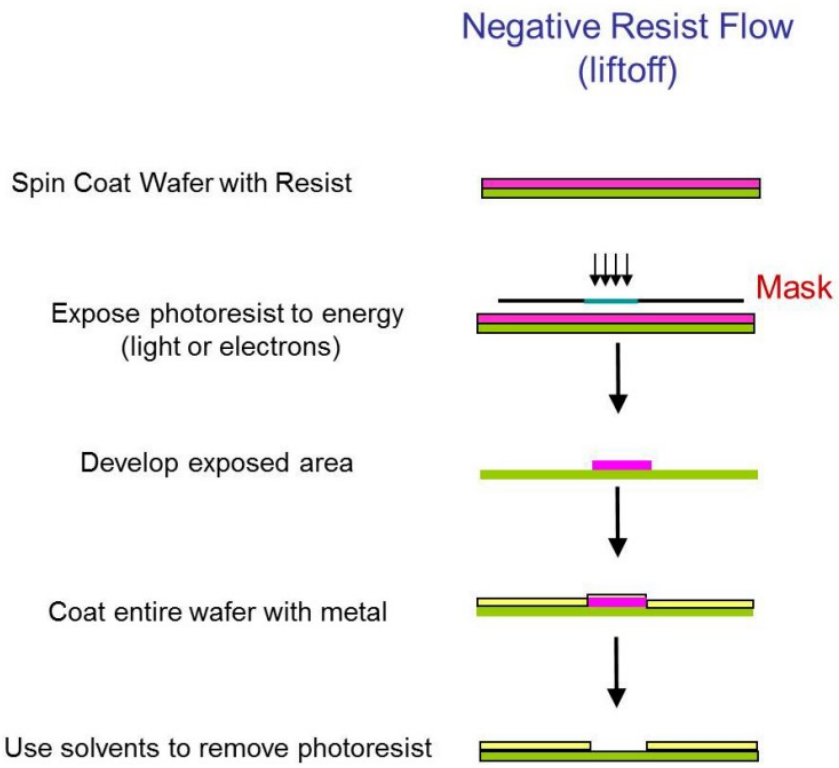

Figure 4. Process used in the fabrication of the array.

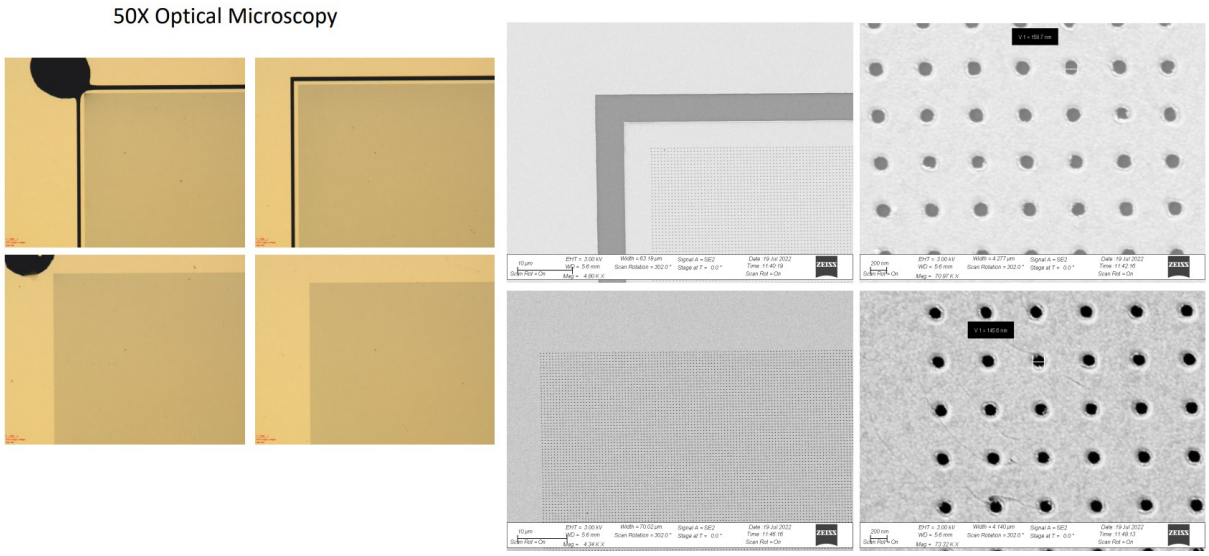

Figure 5. SEM and optical microscopy images of the final array. Images courtesy of Aimee Price, The Ohio State Nanomaterials West Lab.

A 4 inch x 4 inch holder for the array (Appendix B-1) with a 0.1 inch square recess, 8-32 corner bores, and through holes fitted to the area of the array was designed in SolidWorks® (Dassault Sytémes) and 3D-printed in polylactic acid using an Ultimaker™ S5 printer. The holder was clamped to a breadboard using 6 inch optical posts (THORLABS®) and 8-32 screws. The setup can be seen in Figure 6.

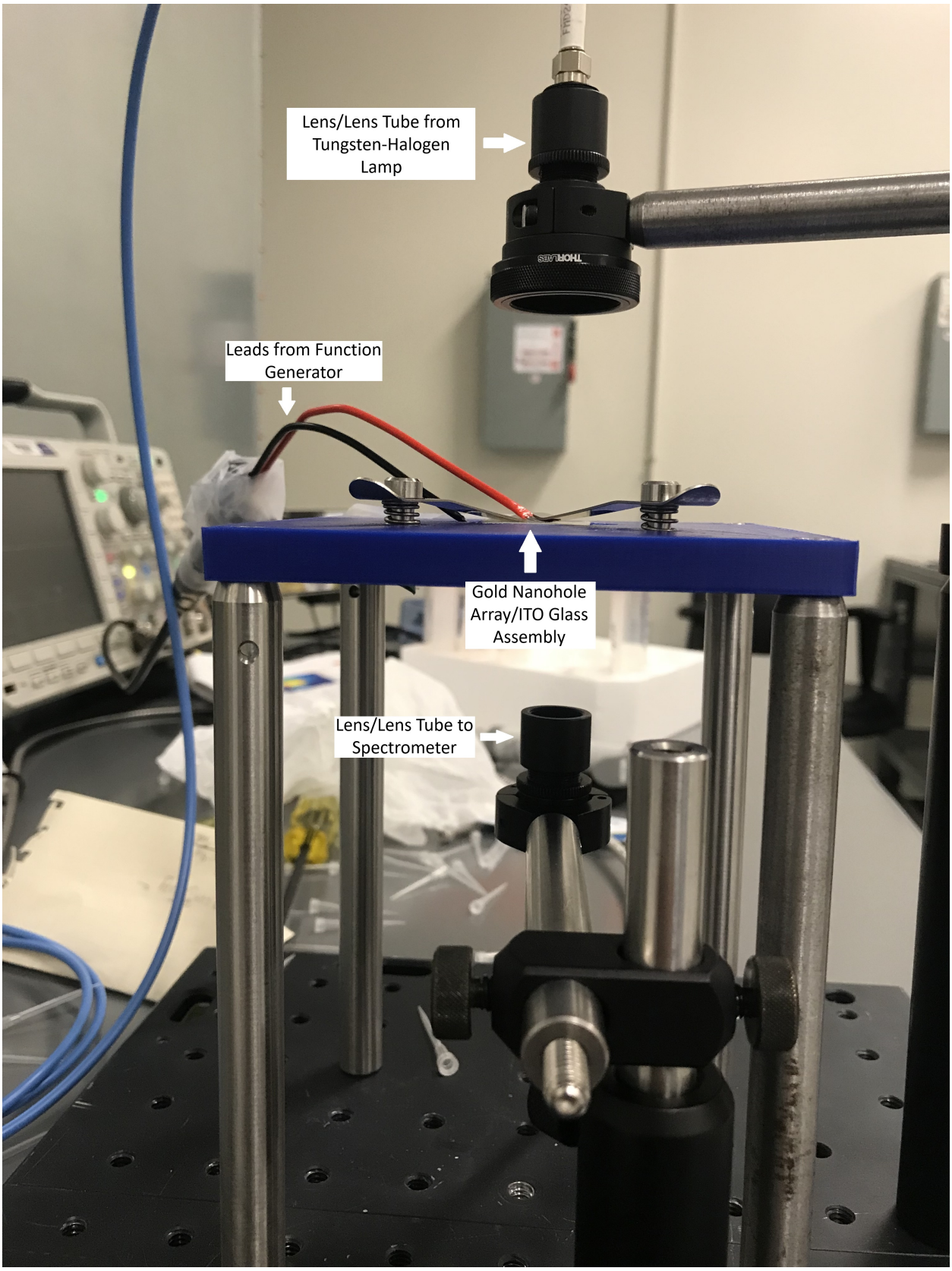

Figure 6. The actual experimental setup as depicted in Figure 3.

The gold array was placed into the 0.1 inch recess of the holder. The conductivity of the water used for the bead suspension was measured to be 1128 mS. The analytes chosen for analysis were polystyrene nanospheres (100 nm, 1% weight per volume in deionized (DI) water, Polysciences®). The PS nanospheres were diluted to twice their volume and placed on the surface in 5 μL aliquots using a micropipette (Eppendorf Research® plus 10 μL). The gold nanohole array was clamped against an indium tin oxide (ITO)-coated glass slide (SPI Supplies®, 70-100 Ω) with 3M™ 1/2 inch width transparent tape (58 μm thickness) covering the side of the ITO slide in contact with the gold.

The sample was illuminated with a tungsten-halogen lamp (Ocean Optics® LS-1, and later THORLABS® OSL2IR) as shown in Figure 3. The lamp light was placed at the focal length of an achromatic lens (THORLABS®, focal length = 19 mm, 1/2 inch achromatic doublet, anti-reflective coating: 400 - 1100 nm) using an Ocean Optics® P400-2-VIS-NIR fiber optic cable and projected onto the sample holder. The transmittance spectrum was then collected by an identical achromatic lens and sent to an Avantes® Avaspec-ULS2048-XL-EVO spectrometer equipped with a 10 μm entrance slit using an Avantes® FC-UVIR600-2 optical fiber. The full width half maximum resolution of this spectrometer configuration is 0.25-0.31 nm.

An alternating current sine wave signal was introduced between the gold and an ITO glass slide using a Hewlett-Packard® 8111a function generator. The function generator was connected to a Tektronix® MDO3024 oscilloscope at the middle terminal of a three way BNC adapter. The signal was then terminated into 2 BNC leads which were stripped, soldered (60:40 Sn:Pb flux), and pounded thin to reduce the electrode gap. The positive lead was clamped on top of the ITO slide, and the negative lead was clamped against the gold layer with THORLABS® SLH1 microscope clips as shown in Figure 3. The oscilloscope was used to monitor the AC signal. The signal frequency was varied and the transmission spectrum recorded every 10 seconds using the "save spectra periodically feature" in Avasoft8 (Avantes®). In between runs, the array and tape-covered slide were rinsed consecutively with acetone, isopropyl aclohol, and finally DI water and allowed to air dry.

The spectrum of a film of water on the array was taken to establish a baseline for the array structure itself. This spectrum was monitored for changes in order to rule out array breakdown as a cause of any change in behavior. High voltage effects were probed by applying a 289 V DC voltage to the array setup using a GW Instek® GPR-30H10D power supply. 20 μL of nanospheres at 0.5% weight per volume were introduced to the gold array and exposed to 289 V for 10 minutes. The nanospheres were then collected, allowed to rest for 5 minutes, then returned to the array. Both baseline and 1 kHz DEP shift behavior was collected for exposed nanospheres in 10 minute intervals. It was found that the process of removing the nanospheres itself changes the behavior of the nanospheres. To correct for this, the nanospheres were placed on the array for 10 minutes, removed and allowed to rest for 5 minutes, and then finally returned to the array for 10 minutes. The increase in shift recorded during the post-removal run was subtracted from shifts collected after exposure to an electric potential.

The procedure reported by Barik et al. was used to analyze shifts in the transmission spectrum of the gold array [9]. After collection, data from the spectrometers in the Avantes® RAW8 file format

was parsed using the *readRAW8* function in the MATLAB® file exchange [13]. The data was then analyzed using a script in MATLAB® which fits a 7th-order polynomial to the region between 800 nm and 900 nm and finds the minimum by setting the derivative equal to zero near the query point of 840 nm. A for loop repeats this process for each data point spaced 10 seconds apart, and then plots the values as a function of time, as can be seen in figures 9, 10, and 11. A 7th-order polynomial was chosen to contain more points of inflection for a better fit, this method produced a mean R^2 value of $0.80 \pm 0.20, N = 12$. A representative polynomial fit of the spectrum may be seen in Figure 7. MATLAB® has the capability of computing polynomial fits of up to 9th degree, however due to the computational rigor of this operation, this was found to produce different results across devices. The shift was also analyzed with a square-root regression (Appendix A.1).

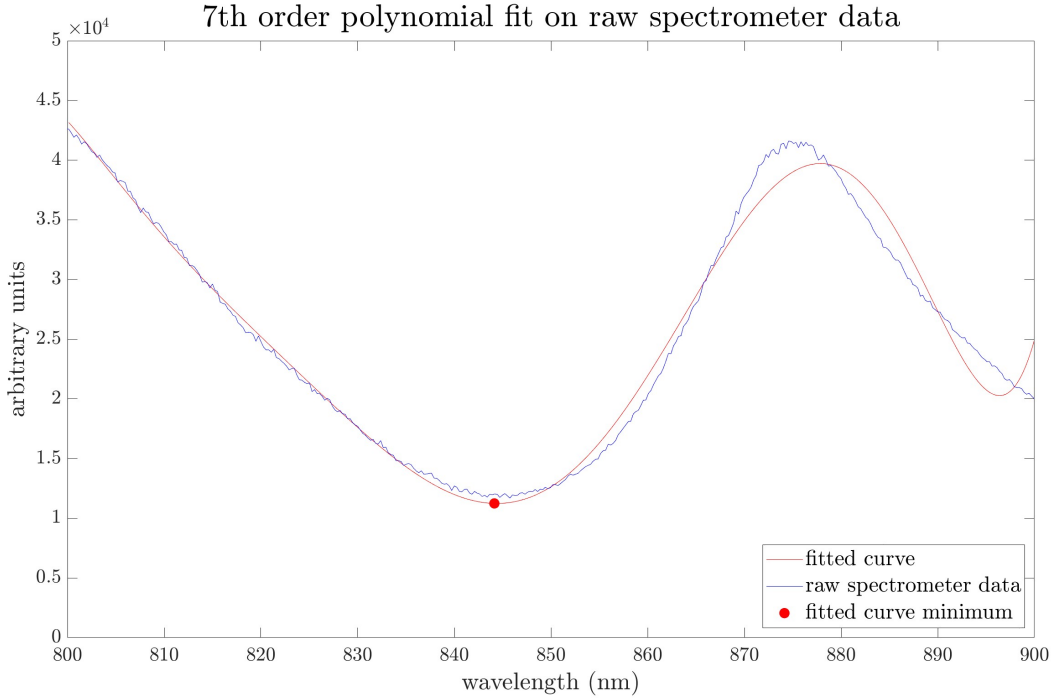

Figure 7. MATLAB polynomial fit to the minimum corresponding to the gold-water interface. The fit was centered around an estimated value of the minimum, 840 nm. To estimate shifts in spectral minima, the polyfit minima were compared.

Several collections were performed with different frequencies at a potential of 36 V peak-to-peak in order to assign positive and negative DEP values. When nearing the crossover frequency, it is necessary to increase the collection time in order to observe an appreciable shift.

To identify the crossover frequency, 10 baselines were conducted with no voltage applied. The resultant shift from each of the runs was fit to a square root function, and the equation recorded. Finally, a frequency was identified that was found to nominally produce the same average equation (and thus average shift) as a baseline with no voltage applied over the same time period. This frequency was used as the crossover frequency.

To probe for particle breakdown, a 5 μL aliquot of the nanospheres was subjected to 289 V DC for 10 minutes. The function generator was unable to produce a voltage above 36 V AC without an amplifier, so a DC power supply was used instead. Due to time constraints, the voltage was directly increased to 289 V from 36 V, as the nanospheres showed no change after the 36 V AC exposures. After the 289 V DC exposure, the nanospheres were collected, allowed to rest for 5 minutes, and then finally reintroduced to the array for subsequent baseline and 1 kHz 36V peak-to-peak runs.

Simulations of both the electric field and the electric field gradient were performed in MATLAB® using the PDE Toolbox. Depictions of the DEP force and torque were then calculated (Figures 18 and 19). Laplace's equation was solved using the finite element method for the area above a single nanohole and the electric field taken as the gradient of electrostatic potential. The hole geometry of 160 nm in diameter and 600 nm center-to-center spacing was used for the model. The electrode gap was taken as the tape thickness listed by the manufacturer (58 μm). This resulted in values for the electric field. In order to find the gradient of the electric field, the solution to the Laplace equation for electromagnetism was interpolated in a 300 nm wide by 200 nm tall grid in the region of the hole with x coordinates spaced 1.5 nm apart and y coordinates spaced 1 nm apart. Constant spacing was necessary as it is a requirement for the MATLAB® gradient function. The actual code used is provided in Appendix A.3.

5.0 RESULTS

The collected SPR spectrum can be seen in Figure 8. The valley and peak near 840 nm and 850 nm respectively correspond to the gold-water interface [9]. In the absence of water, the spectrum instead takes the form of two peaks, as the gold-water interface is absent.

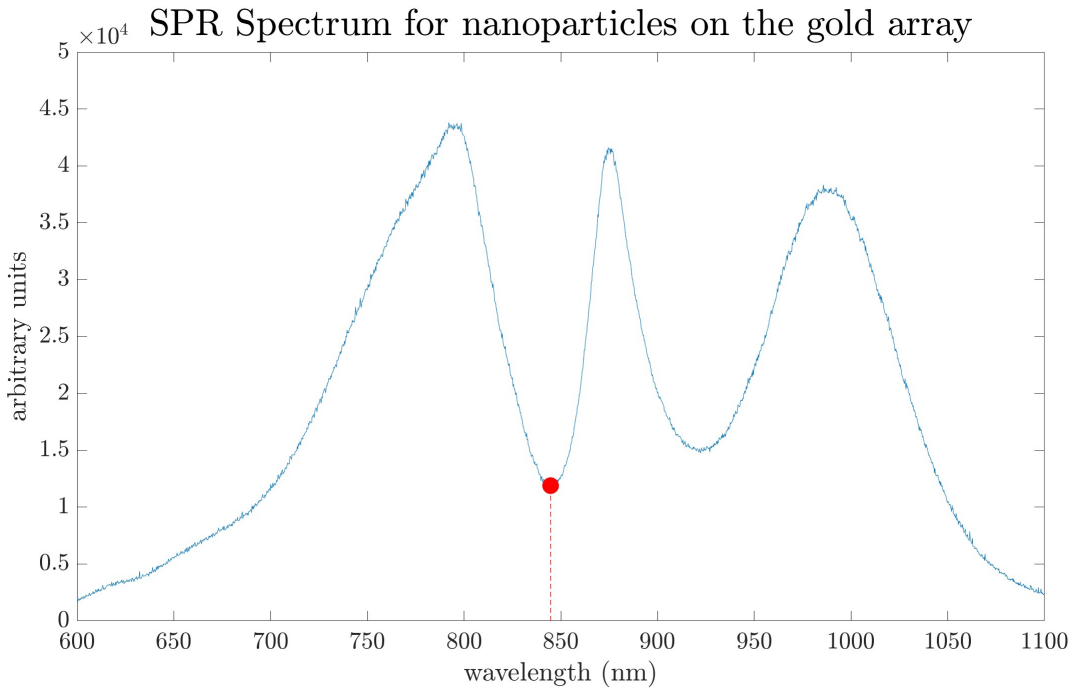

Figure 8. Observed SPR spectrum for polystyrene nanospheres on the gold nanohole array. The minimum near 840 nm, identfied here by the red point, corresponds to the gold-water interface. During DEP cycles, this minimum is tracked and the shifts in wavelength for the minimum indicate DEP forces acting on the nanospheres.

Positive DEP was characterized by a shift in the valley near 840 nm wavelength towards longer wavelengths (see Figure 9). Frequencies corresponding to negative DEP restored the collected spectrum to baseline peak energies. Reversible binding due to positive and negative DEP was observed in a frequency range of 1 kHz - 22.4 MHz (Figure 9). Some exposures produced a shift below the resolution of the spectrometer, however, these shifts are reversible, frequency-dependent, and agree with the theory of DEP-induced binding. This indicates some degree of resolution in the observed frequency shift range. Nanospheres from the stock solution (1% weight per volume) that were deposited on the array and subjected to a voltage of 36.0 V AC peak-to-peak displayed repeated periods of positive and negative DEP when the frequency was alternated between 1 kHz and 22.4 MHz respectively. However, a solution diluted to half the original concentration did not display any evidence of negative DEP. Supplied voltages below 36 V peak-to-peak produced smaller shifts that were difficult to resolve. The reversibility of the shift when large frequency changes are made indicates DEP-based binding of polystyrene to the gold surface.

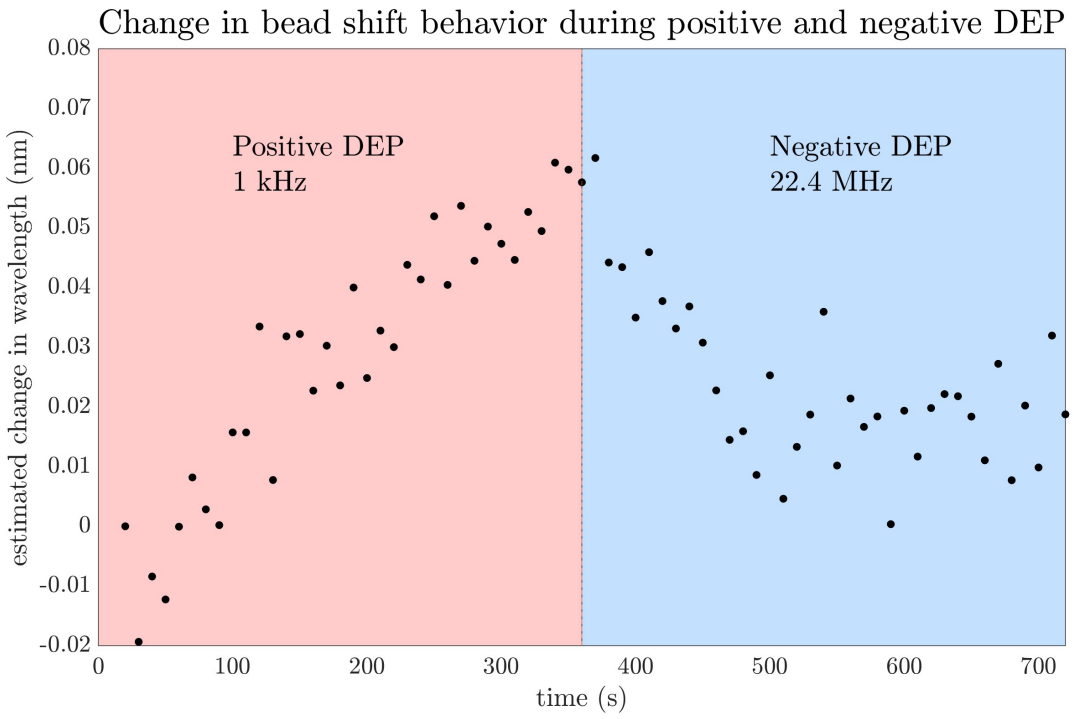

Figure 9. Positive and negative DEP cycle. Positive DEP was established by applying an AC electric field to the nanospheres at 1 kHz, while negative DEP was a result of setting the electric field to 22.4 MHz. The frequency of the applied field was changed at time t = 360 s, as indicated by the color change from red to blue. The shift was recorded in intervals of 10 seconds and the data points correspond to the minimum of the polynomial fit of the transmission spectrum through the gold array.

The region of frequencies near 10.95 MHz is characterized by little to no DEP-induced valley shift. Instead, at these frequencies the spectrum appears to show a slow, time-dependent shift due to diffusion. A baseline with no voltage applied can be seen in Figure 10, which shows a shift in the spectrum due to diffusion.

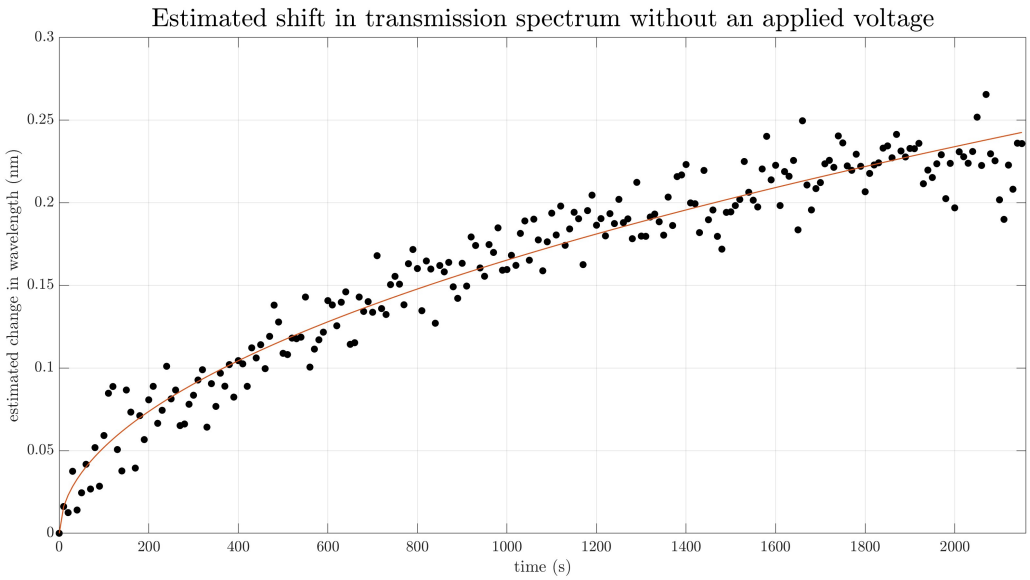

Figure 10. Shift in the polynomial fit of the transmission spectrum due to diffusion. Polystyrene nanospheres were placed between the electrodes with no electric field applied. Note the longer time needed for spectrum shifts due to diffusion.

Baseline measurements were found to mathematically agree with the expected behavior of one-dimensional diffusion of analytes with irreversible binding through the relevant equation governing this type of behavior

$$\Gamma(t) = 2C_{bulk}\sqrt{\frac{Dt}{\pi}} \tag{6}$$

Equation 6. Surface coverage of an analyte undergoing one-dimensional diffusion with irreversible binding

where Γ(t) is the surface coverage at a given time t, C_{bulk} is the bulk concentration of the analyte, and D is the diffusion coefficient of the analyte [14].

The enhanced detection due to DEP can be seen in Figure 11, as the shift in transmission spectrum increases when a positive DEP force is applied.

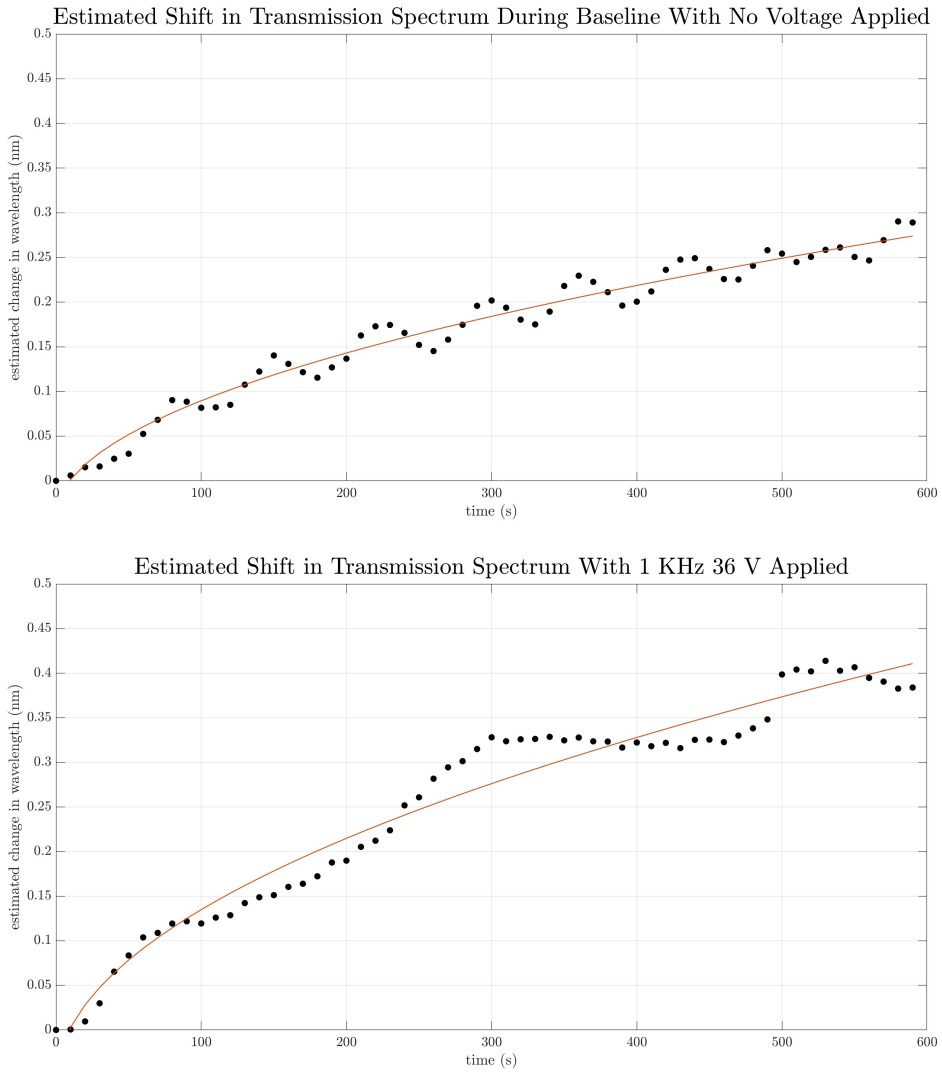

Figure 11. Behavior of nanospheres due to DEP and electro-osmotic forces before being exposed to 289 V DC. Top: the shift in the polynomial fit of the spectrum when no voltage is applied to the nanospheres over 10 minutes. Bottom: the shift in the polynomial fit of the spectrum when 36 V at 1 kHz is applied to the nanospheres over 10 minutes. The red lines represent the square-root fit.

A change in both the DEP and diffusive behavior of the nanospheres was observed after being exposed to large voltages. The effects of high voltage exposure on bead behavior are summarized in Table 1.

Table 1. Effects of a 289 V peak-to-peak exposure on estimated spectral shift over the same time period (10 minutes). Values shown are the average of 3 runs under identical experimental conditions with their standard deviations.

Baseline Type	Shift Before Exposure (nm)	Exposure Type	Shift After Exposure (nm)
No Voltage	0.26 ± 0.02	None (Baseline)	0.82 ± 0.11
No Voltage	0.26 ± 0.02	289 V DC	1.56 ± 0.27
36 V 1 kHz	0.38 ± 0.04	289 V DC	1.21 ± 0.11

These results show a qualitative modification of the described experimental setup as a whole. This modification is further illustrated in Figures 12-14. The mechanism of this change cannot be identified to be electrical, as removal and reintroduction of the nanospheres to the gold array in itself modifies their behavior.

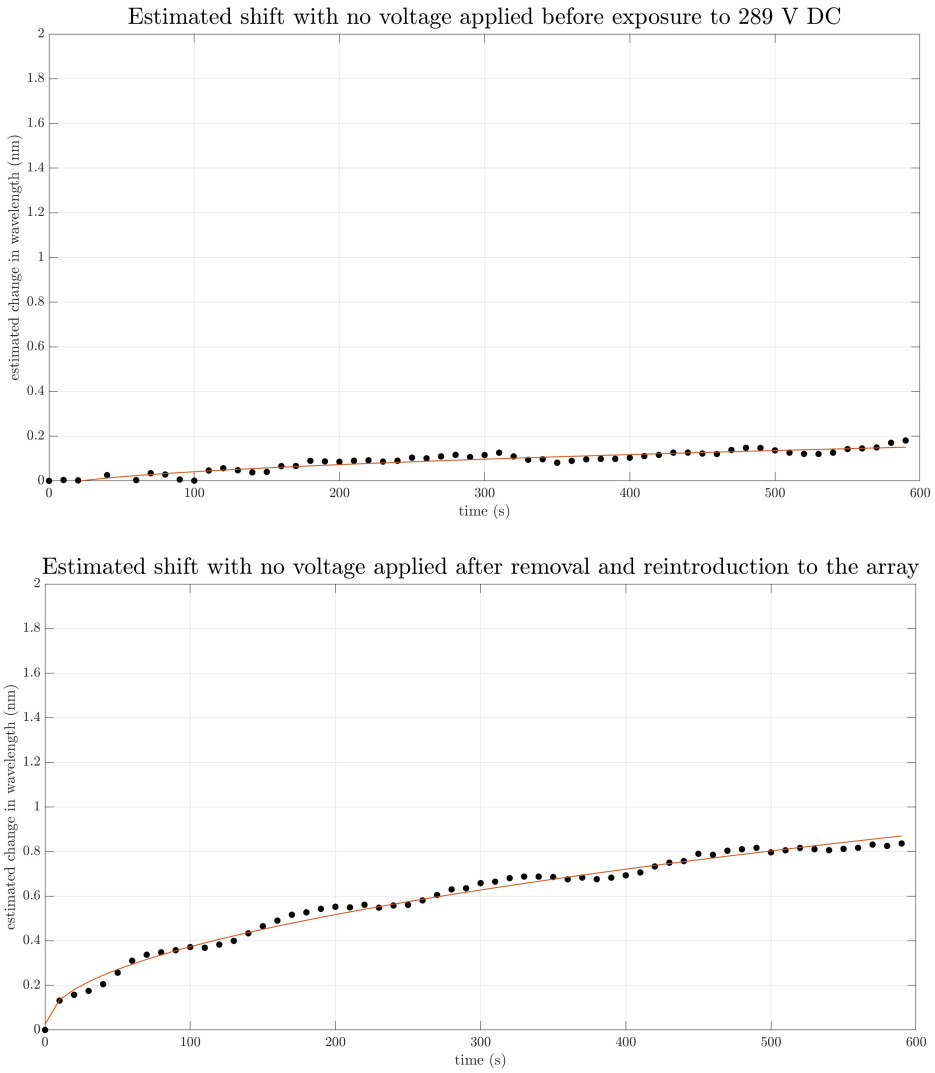

Figure 12. Plot showing one set of experimental runs using the parameters in the 1st row of Table 1 and displaying effect of removing and reintroducing the nanospheres to the array via micropipette. Shown in red is a square root fit for illustrative purposes.

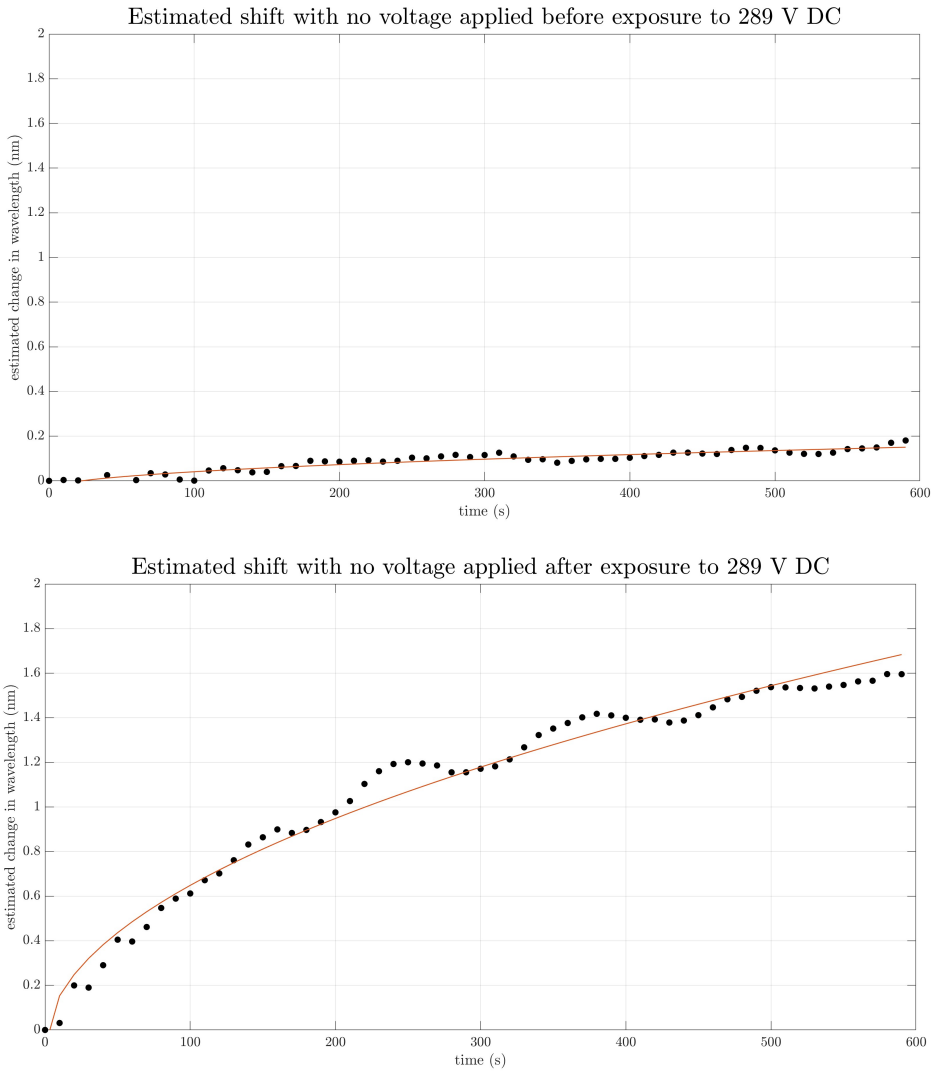

Figure 13. Plot showing one set of experimental runs using the parameters in the 2nd row of Table 1 and displaying effect of 289 V DC on the diffusive behavior of the nanospheres. Shown in red is a square root fit for illustrative purposes.

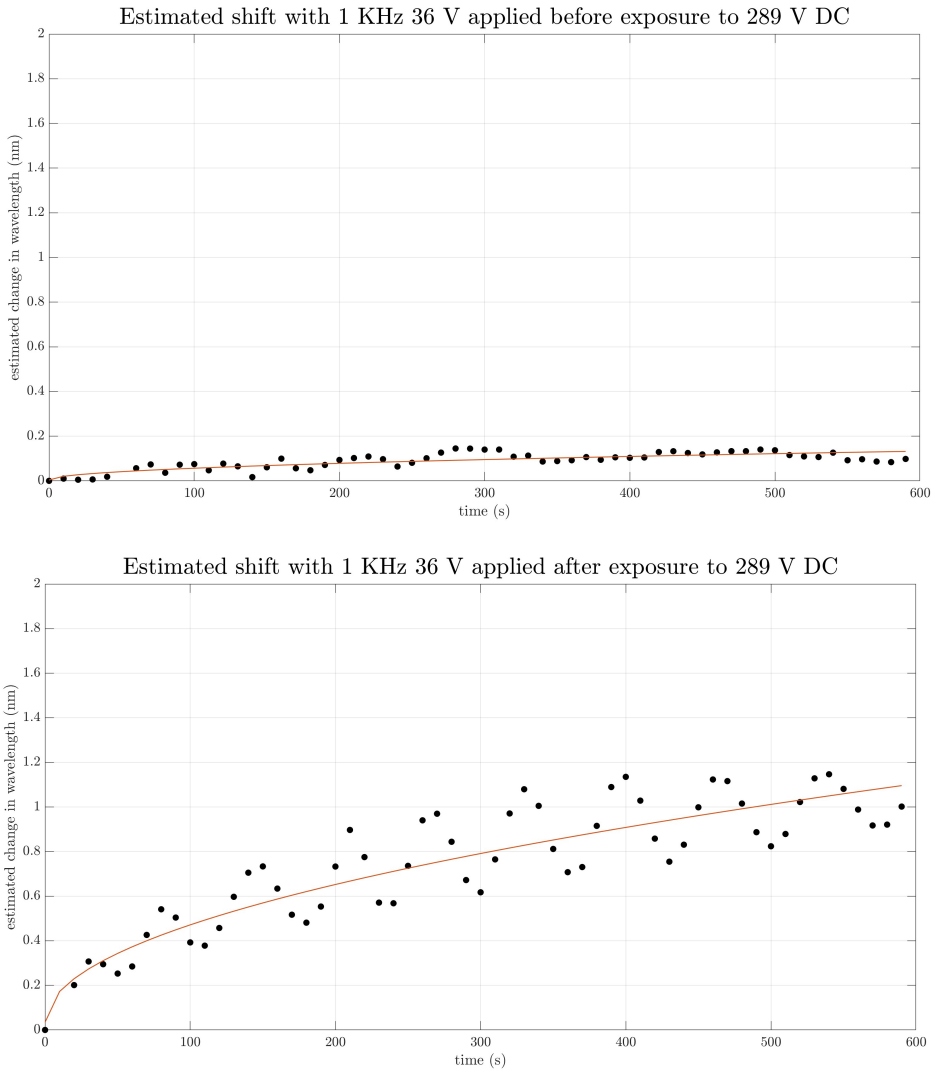

Figure 14. Plot showing one set of experimental runs using the parameters in the 3rd row of Table 1 and displaying effect of 289 V DC on the behavior of the nanospheres during positive dielectrophoresis. Shown in red is a square root fit for illustrative purposes.

To identify the crossover frequency, 12 baselines were conducted with no voltage applied. The resultant shift from each of the runs was fit to a square root function, and the equation recorded. Finally, a frequency was identified that was found to nominally produce the same average equation (and thus average shift) as a baseline with no voltage applied over the same time period. This frequency is used as the crossover frequency, with the standard deviation of the mean of the 12 runs as the standard uncertainty. This method resulted in an estimated crossover frequency of 10.95 ± 3.232 MHz. The square root fitting process resulted in a relative standard uncertainty of 0.2952 nm for runs where no voltage was applied and 0.2710 nm for runs with a frequency of 10.95 MHz applied. Given the considerable relative uncertainty in determining the crossover frequency, equations and subsequent figures which make use of this value (Figures 15-19) are illustrative of

the qualitative behavior of particles subject to DEP and do not reveal any quantitative material properties of the nanospheres.

The conductivity of the polystyrene nanospheres was solved for using Equation 4 by using the experimentally determined crossover frequency of 10.95 MHz $\pm$ 3.232 MHz. This resulted in a conductivity value of $6.6 \times 10^{-2} \pm 8.7 \times 10^{-4}$ S. The experimental conductivity value is higher than the expected value for pure PS (2.5 ε, 2.2135×10^{-11} F/m) [8]. Consequently, the conductivity of the nanospheres can be understood as being solely due to the electrical double layer that forms at the particle-solution boundary [8], [15]. Using the measured conductivity of the PS nanospheres, one can determine the real part of f_{CM} as a function of frequency using a relation by Mortadi [5]:

$$Re[f_{CM}] = \frac{\omega^2(\varepsilon_p - \varepsilon_m)(\varepsilon_p + 2\varepsilon_m) + (\sigma_p - \sigma_m)(\sigma_p + 2\sigma_m)}{\omega^2(\varepsilon_p + 2\varepsilon_m)^2(\sigma_p + 2\sigma_m)^2}. \tag{7}$$

Equation 7. Real portion of the Clausius-Mossotti function

This result enables the prediction of the dielectrophoretic behavior of the PS/water system and enables the determination of the frequency-dependent dielectrophoretic force for a given location in the system. The force is obtained from Equation 2. Additionally, the torque on the nanospheres may be calculated using Equation 3 and another relation by Mortadi [5]:

$$Im[f_{CM}] = \frac{\omega(\sigma_m - \sigma_p)(\varepsilon_p + 2\varepsilon_m) - (\varepsilon_p - \varepsilon_m)(\sigma_p + 2\sigma_m)}{\omega^2(\varepsilon_p + 2\varepsilon_m)^2 + (\sigma_p + 2\sigma_m)^2}. \tag{8}$$

Equation 8. Imaginary portion of the Clausius-Mossotti function

The result of substituting the experimental conductivity value for the polystyrene nanospheres into Equations 7 and 8 may be seen in Figure 15.

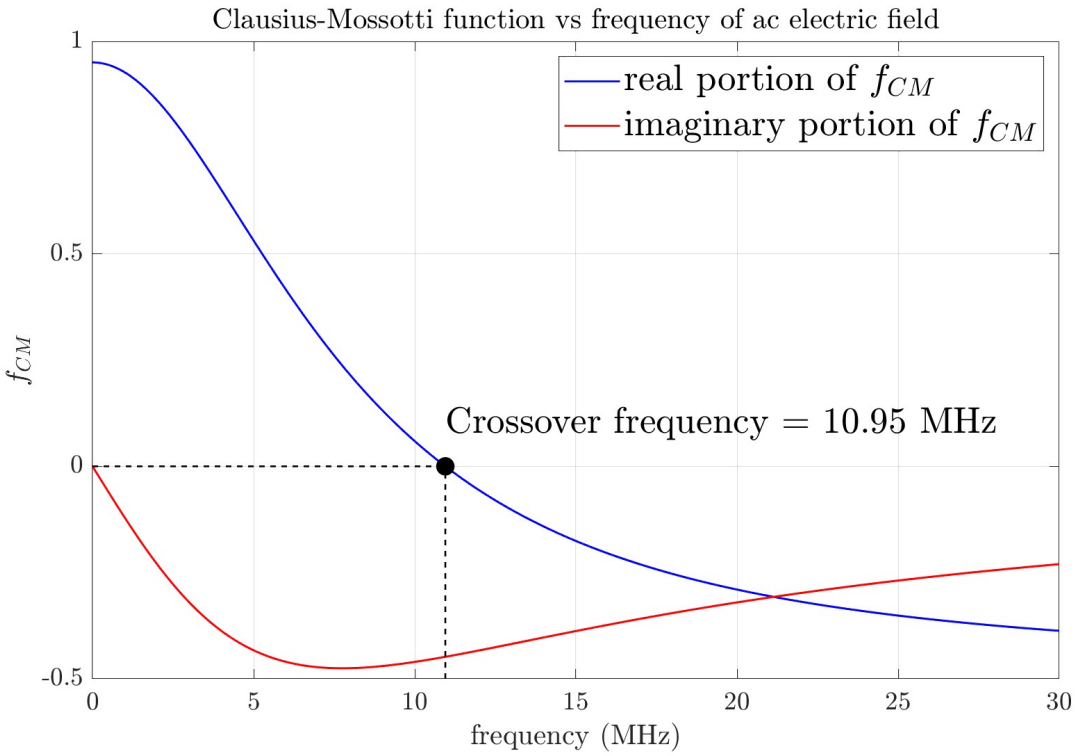

Figure 15. Graph of the real and imaginary portions of the Clausius-Mossotti function and the measured crossover frequency.

A query point at 45 degrees to the nanohole corner and a particle radius (50 nm) away was selected to illustrate the effect of frequency on the theoretical DEP force and torque on a nanosphere near the gold array. The results of this process for an applied voltage of 289 V DC are shown in Figures 16 and 17.

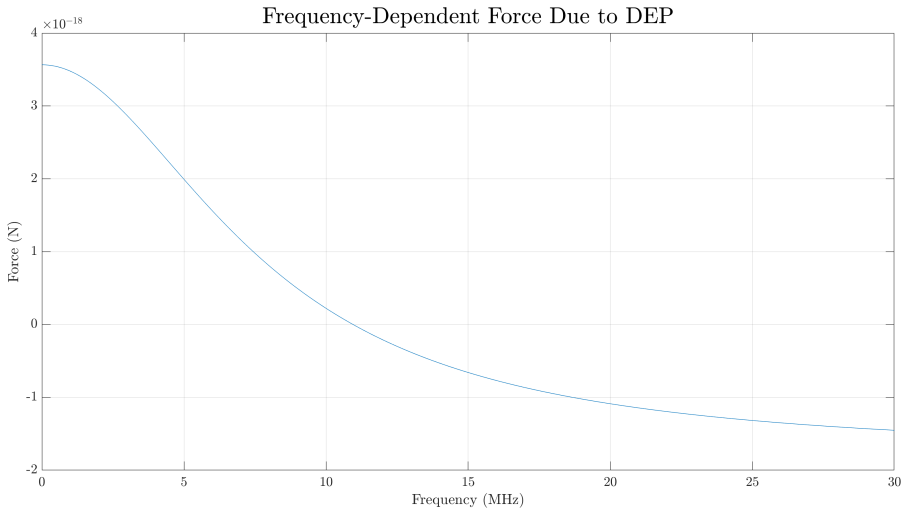

Figure 16. The theoretical effect of frequency on DEP force at the point (-44nm, 135nm) in the finite element model geometry for an applied voltage of 289 V DC.

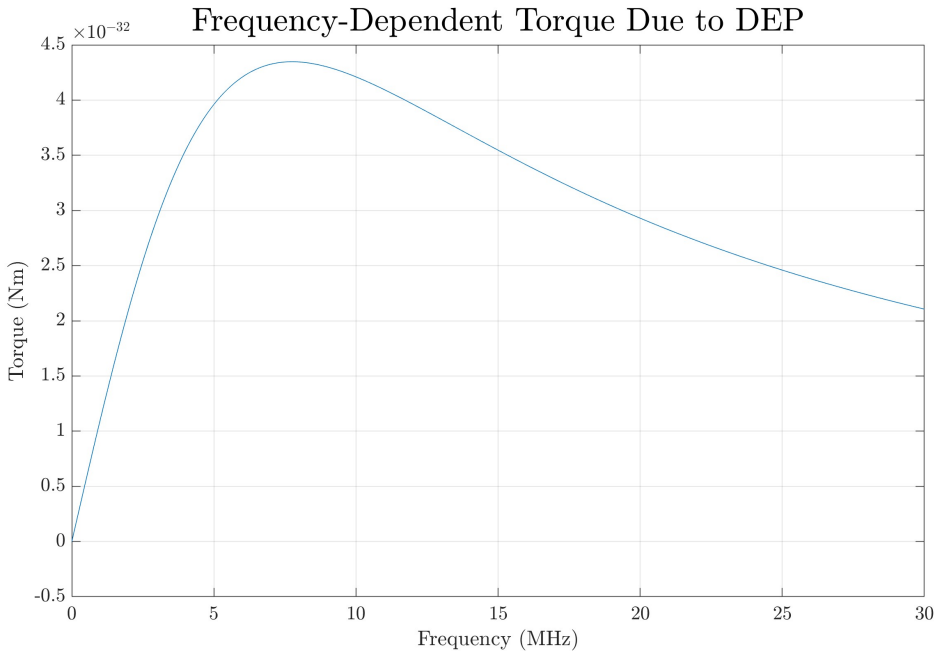

Figure 17. The theoretical effect of frequency on DEP torque at the point (-44nm, 135nm) in the finite element model geometry for an applied voltage of 289 V DC.

Additionally, the spatially resolved DEP force and torque may be calculated using Equations 2 and 3. The result of this procedure can be seen in Figures 18 and 19.

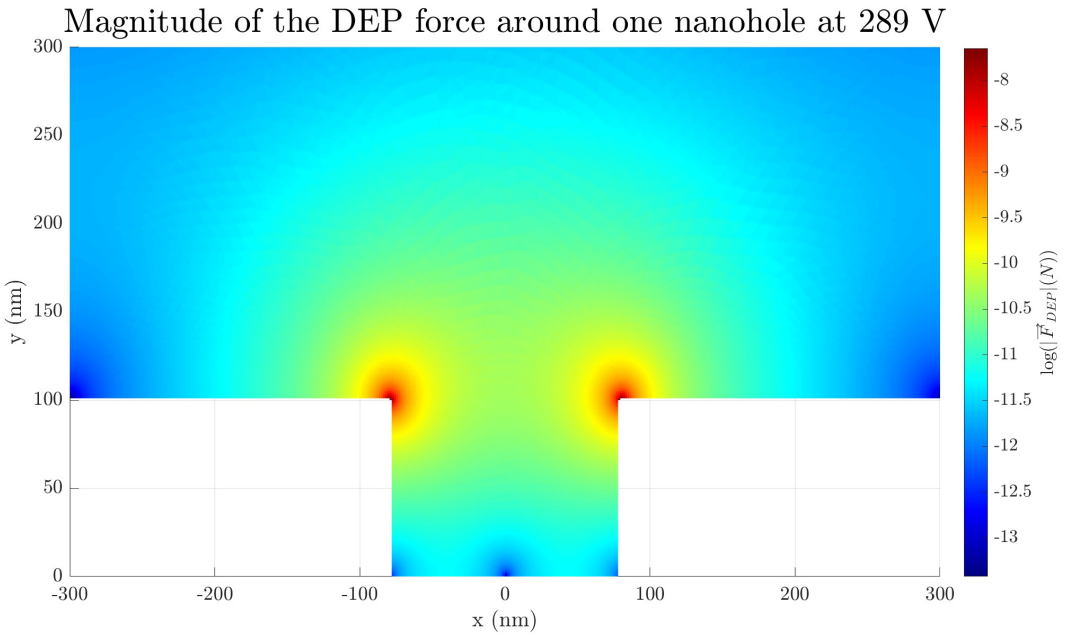

Figure 18. Dielectrophoretic force experienced by a particle around one nanohole.

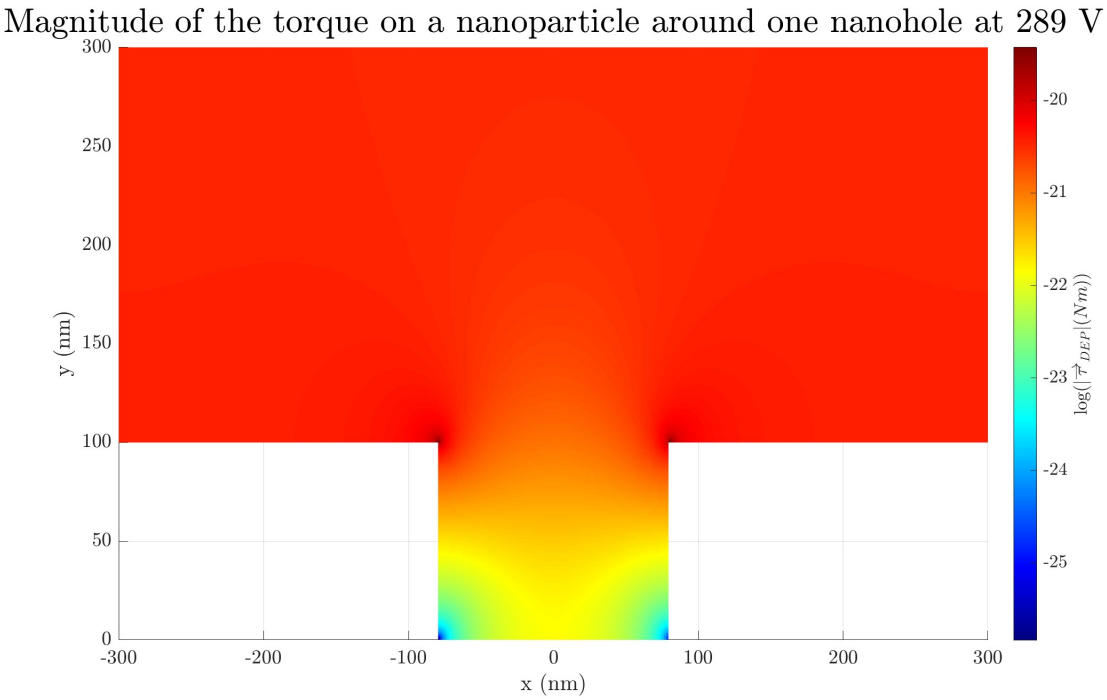

Figure 19. Dielectrophoretic torque experienced by a particle around one nanohole.

As the observable shift is near the full-width-half-maximum resolution of the spectrometers that

were used, several steps were taken in order to verify these results. The same spectrometer settings (integration time and averages) were used for each collection used in the determination of the crossover frequency. This allowed a comparison between the fits of each run. The same voltage was applied for DEP-induced spectral shift measurements. This allowed the total shift to then be compared between these runs. These findings indicate a frequency-dependent shift whose sign agrees with theory.

6.0 DISCUSSION

A change in the behavior of the polystyrene-gold system was observed after being exposed to 289 V DC. An increase in spectral shift due to polystyrene binding during no voltage applied and dielectrophoresis runs was observed. After exposure to 289 V DC, the resulting shift observed with the nanosphere spectrum nearly doubled in comparison to the shift with no voltage exposure. This may indicate voltage-induced modulation of a non-electrical property.

Runs where the nanospheres were not exposed to a voltage show an increase in spectral shift after being removed and replaced, as seen in the first row of Table 1. Aggregation of agitated micro and nanospheres is a known consequence of their use [16]. Consequently, an increase in baseline spectrum shifts can be explained by DEP-induced aggregation. DEP has also previously been found to be capable of particle chaining. Additionally, when used in conjunction with high voltage DC currents, chains of nanospheres may be fused together [17]. A field-induced permanent aggregation of the polystyrene nanospheres would increase baseline shifts due to the dependency of settling velocity on particle diameter (see Equation 9, where v is the settling velocity, d is the diameter of the particle, g is the gravitational acceleration constant, ρ_p is the density of the particle, ρ_f is the density of the fluid, and η is the dynamic viscosity). This increase in spectral shift would also manifest itself in DEP runs, as the same dependency exists for the DEP force. It is unknown whether the observed permanent change in estimated wavelength shift is in fact due to aggregation as this notion was not investigated further using other analytical methods. Interestingly, the micro-pipetting process itself seems to induce an aggregation in the nanospheres tested.

$$v = \frac{d^2 g(\rho_p - \rho_f)}{18\eta}. \tag{9}$$

Equation 9. Settling velocity of a sphere in fluid

Throughout experimentation, several array designs were used. The array designs did not appear to significantly influence the behavior of the nanospheres.

Additional difficulty was encountered in the cleaning of the array. After rinsing the array with acetone and isopropyl alcohol, a small amount of white residue remained. In an attempt to remove the residue, the gold nanohole array was submerged in acetone and sonicated. However, some of the gold lifted off the titanium layer. Throughout experimentation, the adhesion of the gold to titanium was found to be mechanically susceptible to failure. The weakness of the gold-titanium interface limited all cleaning to simple rinsing with acetone, isopropyl alcohol, and DI water. Residual material on the sample could be due to aggregation of the PS, which may negatively

affect its solubility in the rinsing solvents.

During preliminary testing, additional minor peaks in the valley near 840 nm were observed. After several runs, however, these peaks diminished and did not return. This may indicate the presence of remnants from the gold array fabrication process, and these spectra are not considered in the experimental data.

During experimentation, a slow, irreversible positive wavelength shift was observed in the valley near 840 nm. This phenomenon has been observed before [9] and may be a result of a dirty gold surface. Although gold is resistant to chemical attacks, it has a high surface energy characteristic of transition metals which makes it susceptible to surface binding events from organic compounds [18]. This phenomenon may explain the observed persistent spectral shift. Placing the array in a beaker of acetone and spinning by hand successfully reversed the shift. Any small change in the valley near 830 nm due to dirtying does not affect the reported measurements since the shift is measured relative to the starting wavelength value for the valley.

Additionally, a gradual increase in total spectral shift was observed during experimentation. This may be explained mechanistically by mechanical breakdown of the gold layer, as it has been shown previously that irregular metal surfaces enhance plasmonic transduction [19].

As seen in Figure 11, some runs exhibited a random sinusoidal fluctuation in spectral shift that appeared to be superimposed on the expected positive shift. This result is unexpected and appears to be unreported in the literature. A possible explanation for this observed behavior is a convection current driving the beads closer and further to the gold array in a periodic fashion. This convection current may be a result of a temperature gradient between the gold array and top ITO slide. Extended exposure to the tungsten-halogen lamp may lead to this difference in temperature. The temperature difference could also arise from the cleaning process wherein the gold and ITO slide are rinsed with isopropyl alcohol, and thus possibly evaporatively cooled. If due to convection currents, this sinusoidal behavior may be able to be diminished by resting the array and ITO for 10 minutes after cleaning to return them to thermal equilibrium.

Another possible source of error identified in this setup is the gap between the electrodes. Due to the clamps needing to be placed by hand each time, their placement varied slightly each run. Differences in clamp placement leads to variable electrode gaps at different points in the sensor. Small differences in the electrode gap may lead to large differences in the DEP force, as can be seen in Equation 5. This source of error also contributes to variability in pure diffusion measurements as it changes the distance required for diffusion slightly each run. In order to circumvent this, the area of the ITO glass electrode was reduced. Thus, the function generator leads were able to be placed without interference, and the electrodes could rest flush against each other. This modification, along with the increase in spectrometer resolution, led to increased reliability between runs, as well as more quantifiable results. There is also still an open question on the ultimate precision allowed by the fitting of the experimental spectra with a polynomial and tracking the inflection point during the experiment. Future studies should evaluate/measure the baseline shift with time with no voltage applied and at varying times throughout the day when background temperatures might slightly shift to quantify drift.

While the described setup is designed to minimize any evaporation of the solution, some evaporation may still occur. If evaporation is present, it can lead to variations in the collected measurements, particularly those with longer collection times as it effectively changes the concentration of the analyte solution.

7.0 CONCLUSIONS

The original work by Barik et. al. provided little detail as to the exact experimental procedure used, thus inferences as to the polynomial fitting parameters and gold array fabrication process had to be made. While a DEP-based sterilization instrument seems possible in theory, its application would be severely limited due to spatial and fiscal limitations. The dependence of the DEP force on the electric field gradient requires miniscule electrode geometries. Furthermore, the DEP force only becomes significant very close to the electrode structure. This fact necessitates passing the affected analyte extremely close to the electrode. In addition, the fabrication methods required to produce micro and nanoelectrodes far exceed the costs associated with alternative sterilization methods such as UV exposure [20].

The presented DEP-enhanced plasmonic sensor presents a significant challenge in implementation due to extreme sensitivity of the experimental design and is thus best suited for non-selective analyte detection. The described setup has potential for applications determining the dielectric properties of biological molecules which could be examined in future work. Additionally, the hypothesis of particle geometry modulation may be investigated by examining particles which have been exposed to high potentials within the instrument with a suitable microscopy method.

8.0 RECOMMENDATIONS

This procedure for plasmonic detection was found to be incredibly sensitive to spectrometer resolution which should be the first priority in its reproduction. Similar results are possible with spectrometer resolutions greater than 0.31 nm, however, these spectrometers may produce more unreliable results. A reproduction or modification of this process should take into account the major sources of error and the extreme sensitivity of the sensor as identified in this work.

9.0 REFERENCES

1. T. B. Jones, *Electromechanics of Particles*. Cambridge University Press, 1995. DOI: 10.1017/CBO9780511574498 1, 2, 4, 6.

2. M. P. Hughes, H. Morgan, F. J. Rixon, J. P. Burt, and R. Pethig, "Manipulation of herpes simplex virus type 1 by dielectrophoresis," *Biochimica et Biophysica Acta (BBA) - General Subjects*, vol. 1425, no. 1, pp. 119–126, 1998, ISSN: 0304-4165. DOI: https://doi.org/10.1016/S0304-4165(98)00058-0. [Online]. Available: https://www.sciencedirect.com/science/article/pii/S0304416598000580 2.

3. M. P. Hughes, H. Morgan, and F. J. Rixon, "Measuring the dielectric properties of herpes simplex virus type 1 virions with dielectrophoresis," *Biochimica et Biophysica Acta (BBA) - General Subjects*, vol. 1571, no. 1, pp. 1–8, 2002, ISSN: 0304-4165. DOI: https://doi.org/10.1016/S0304-4165(02)00161-7. [Online]. Available: https://www.sciencedirect.com/science/article/pii/S0304416502001617 2.

4. P. Marszalek, J. Zielinsky, M. Fikus, and T. Tsong, "Determination of electric parameters of cell membranes by a dielectrophoresis method," *Biophysical Journal*, vol. 59, no. 5, pp. 982–987, 1991, ISSN: 0006-3495. DOI: https://doi.org/10.1016/S0006-3495(91)82312-8. [Online]. Available: https://www.sciencedirect.com/science/article/pii/S0006349591823128 5.

5. A. Mortadi, A. E. Melouky, E. G Chahid, R. E. Moznine, and O. Cherkaoui, "Studies of the clausius–mossotti factor," *Journal of Physical Studies*, vol. 20, no. 4, p. 4, 2016. DOI: 10.30970/jps.20.4001 5, 22.

6. A. J. Bur, "Dielectric properties of polymers at microwave frequencies: A review," *Polymer*, vol. 26, no. 7, pp. 963–977, 1985, ISSN: 0032-3861. DOI: https://doi.org/10.1016/0032-3861(85)90216-2. [Online]. Available: https://www.sciencedirect.com/science/article/pii/0032386185902162 5.

7. J. Fiedler, M. Boström, C. Persson, *et al.*, "Full-spectrum high-resolution modeling of the dielectric function of water," *The Journal of Physical Chemistry B*, vol. 124, no. 15, 3103–3113, 2020. DOI: 10.1021/acs.jpcb.0c00410 5.

8. K. Khoshmanesh, C. Zhang, S. Nahavandi, *et al.*, "Size based separation of microparticles using a dielectrophoretic activated system," *Journal of Applied Physics*, vol. 108, no. 3, p. 034 904, 2010. DOI: 10.1063/1.3457226. eprint: https://doi.org/10.1063/1.3457226. [Online]. Available: https://doi.org/10.1063/1.3457226 5, 22.

9. A. Barik, L. M. Otto, D. Yoo, J. Jose, T. W. Johnson, and S.-H. Oh, "Dielectrophoresis-enhanced plasmonic sensing with gold nanohole arrays," *Nano Letters*, vol. 14, no. 4, pp. 2006–2012, 2014, PMID: 24646075. DOI: 10.1021/nl500149h. eprint: https://doi.org/10.1021/nl500149h. [Online]. Available: https://doi.org/10.1021/nl500149h 5, 6, 11, 13, 27.

10. A. Ramos, H. Morgan, N. G. Green, and A. Castellanos, "Ac electric-field-induced fluid flow in microelectrodes," *Journal of Colloid and Interface Science*, vol. 217, no. 2, 1999. [Online]. Available: https://eprints.soton.ac.uk/372372/ 5.

11. C.-H. Han, S. Y. Woo, J. Bhardwaj, A. Sharma, and J. Jang, "Rapid and selective concentration of bacteria, viruses, and proteins using alternating current signal superimposition on two coplanar electrodes," *Scientific Reports*, vol. 8, no. 1, p. 14 942, 2018, ISSN: 2045-2322. DOI: 10.1038/s41598-018-33329-7. [Online]. Available: https://doi.org/10.1038/s41598-018-33329-7 5.

12. S. Kim, M. S. Jang, V. W. Brar, Y. Tolstova, K. W. Mauser, and H. A. Atwater, "Electronically tunable extraordinary optical transmission in graphene plasmonic ribbons coupled to subwavelength metallic slit arrays," *Nature Communications*, vol. 7, Aug. 2016. DOI: 10.1038/ncomms12323 5.

13. Y. Jiang, *Avantes8 to Matlab*, Online; accessed July 6, 2022, 2022. [Online]. Available: https://www.mathworks.com/matlabcentral/fileexchange/98339-avantes8-to-matlab 12.

14. D. B. Hibbert, J. J. Gooding, and P. Erokhin, "Kinetics of irreversible adsorption with diffusion: Application to biomolecule immobilization," *Langmuir*, vol. 18, no. 5, pp. 1770–1776, 2002. DOI: 10.1021/la015567n. eprint: https://doi.org/10.1021/la015567n. [Online]. Available: https://doi.org/10.1021/la015567n 16.

15. J. Lyklema and A. d. Keizer, in *Fundamentals of interface and Colloid Science*. Academic Press, 1995, vol. 2, 4.58–4.59 22.

16. S. Shrestha, B. Wang, and P. Dutta, "Nanoparticle processing: Understanding and controlling aggregation," *Advances in Colloid and Interface Science*, vol. 279, p. 102 162, 2020, ISSN: 0001-8686. DOI: https://doi.org/10.1016/j.cis.2020.102162. [Online]. Available: https://www.sciencedirect.com/science/article/pii/S0001868619304816 26.

17. N. Hu, J. Yang, S. W. Joo, A. N. Banerjee, and S. Qian, "Cell electrofusion in microfluidic devices: A review," *Sensors and Actuators B: Chemical*, vol. 178, pp. 63–85, 2013, ISSN: 0925-4005. DOI: https://doi.org/10.1016/j.snb.2012.12.034. [Online]. Available: https://www.sciencedirect.com/science/article/pii/S0925400512013433 26.

18. J. Kang and P. A. Rowntree, "Molecularly resolved surface superstructures of self-assembled butanethiol monolayers on gold," *Langmuir*, vol. 12, no. 11, pp. 2813–2819, 1996. DOI: 10.1021/la951015r. [Online]. Available: https://doi.org/10.1021/la951015r 27.

19. H. Yu, Y. Peng, Y. Yang, and Z.-Y. Li, "Plasmon-enhanced light–matter interactions and applications," *npj Computational Materials*, vol. 5, no. 1, 2019. DOI: 10.1038/s41524-019-0184-1 27.

20. M. Raeiszadeh and B. Adeli, "A critical review on ultraviolet disinfection systems against covid-19 outbreak: Applicability, validation, and safety considerations," *ACS Photonics*, vol. 7, no. 11, 2941–2951, 2020. DOI: 10.1021/acsphotonics.0c01245 28.

APPENDIX A - CODE

The following code was run on MATLAB R2022a. Refer to MATLAB documentation for any errors that may arise.

A.1 Spectrometer Data Parsing and Square-Root Fit

```
clear;

% Select folder with the spectrometer data
path = uigetdir(pwd, 'Select a folder');
files = dir(fullfile(path, '*.Raw8'));

% Define plotting variables
z = length(files);
A = zeros([1 z]);

% Data collection time interval
t = 0:10:10*(z-1);

% Loop through the spectrometer data and find the desired wavelength values
for i = 1:z
    filename = ([path '/' files(i).name]);

    % Read in the spectrometer data using called Avantes8 to Matlab
    [wl,s,d,r,m,file] = readRAW8(filename,0);
    x = wl;
    y = s;

    % Define polynomial fit for the spectrometer data
    tf = excludedata(x,y,'domain',[800 900]);
    fo = fitoptions('Method','NonlinearLeastSquares','Exclude', tf,'StartPoint',[1 1]);
    f1 = fit(x,y,'poly7',fo);

    % Find the minimum wavelength value near 840 nm
    d1 = differentiate(f1,x);
    d = fit(x,d1,"poly6",fo);
    f = @(x) ((d.p1)*(x^6)) + ((d.p2)*(x^5)) + ((d.p3)*(x^4)) + ((d.p4)*(x^3)) + ((d.p5)*(x
    A(i) = fzero(f,840);
end

% Calculate the shift of the minimum wavelength
Ashift = A-(A(1));



% Graph settings
set(0,'defaulttextinterpreter','latex')
figure();
plot(t, Ashift, 'o','Color','black','MarkerFaceColor','black','DisplayName','change in mini
xlabel('time (s)','FontSize',20);
ylabel('change in wavelength (nm)','FontSize',20);
set(gca,'TickLabelInterpreter','latex','FontSize',14);
title('PS bead baseline shift without an applied voltage','FontSize',24);
hold on
```

```
grid on

% Find the square-root fit of the data and calculate the R^2 value
[p,s] = polyfit(sqrt(t), Ashift, 1);
yfit = polyval(p, sqrt(t));
r_squared = 1 - (s.normr/norm((Ashift) - mean(Ashift)))^2;

% Plot the square-root fit with the data
plot(t, yfit,'DisplayName','square-root fit','LineWidth',1);
legend('Interpreter','latex', 'FontSize',18);
```

A.2 Analysis of the Clausius-Mossotti Function

```
% Define constants and material properties
wfac = 4*pi*pi;
ep = 2.5*8.854e-12; % permittivity of particle
em = 78*8.854e-12;  % permittivity of medium
op = 6.609e-2;      % conductivity of particle
om = 1.128e-3;      % conductivity of medium

% Define frequency domain
x = linspace(0, 30e6, 30e4);

% Define the real and imaginary Clausius-Mossotti functions
recm = ((wfac*x.^2)*(ep-em)*(ep+2*em) + (op-om)*(op+2*om))./((wfac*(x.^2)*(ep+2*em)^2+(op+2
imcm = ((2*pi*x).*(om-op)*(ep+2*em) - (ep-em)*(op+2*om))./((wfac*x.^2).*(ep+2*em)^2 + (op +

% Plot both parts of the Clausius-Mossotti function
figure();
set(0,'defaulttextinterpreter','latex')
a = plot(x/1e6,recm,"Color",'b','LineWidth',1,'DisplayName','real portion of $f_{CM}$');
hold on
b = plot(x/1e6,imcm,'Color','r','LineWidth',1,'DisplayName','imaginary portion of $f_{CM}$'
xlabel('frequency (MHz)','FontSize',32);
ylabel('$f_{CM}$','FontSize',32);
title('Clausius-Mossotti function vs frequency of ac electric field','FontSize',50);
set(gca,'TickLabelInterpreter','latex','FontSize',14);
grid on

% Find the crossover frequency
diff = 1;
for i = recm
    if abs(i) < diff
        diff = abs(i);
    end
end
xpt = x(find(recm == -diff))/1e6;

% Plot the crossover frequency point
hold on
N=100;
V=zeros(N,1);
plot(linspace(0,xpt,100),V,'--','Color','black','LineWidth',1);
plot(V + xpt,linspace(-0.5,0,100),'--','Color','black','LineWidth',1);
```

```
scatter(xpt,0, 100,"black","filled",'LineWidth',2);
legend([a b],'Interpreter','latex','FontSize',20);
label = {'Crossover frequency = 10.95 MHz'};
text(1.095e7/1e6, 0.1, label,"FontSize",20);
```

A.3 FEM of the Electric Field and Electric Field Gradient Around One Nanohole

```
% Set up the geometry of the nanohole.
gd = [3 3 3;
    4 4 4;
    -3e-7 -3e-7 8e-8;
    3e-7 -8e-8 3e-7;
    3e-7 -8e-8 3e-7;
    -3e-7 -3e-7 8e-8;
    0 0 0;
    0 0 0;
    58e-6 1e-7 1e-7;
    58e-6 1e-7 1e-7];
sf = 'R1-R2-R3';
ns = [82 82 82;
    49 50 51];

% Create a MATLAB FEM model from the nanohole geometry.
model = createpde("electromagnetic","electrostatic");
g = decsg(gd,sf,ns);
gm = geometryFromEdges(model,g);

% Supply electrostatic parameters for the MATLAB FEM solver
pdegplot(gm,"EdgeLabels","on","FaceLabels","on",'VertexLabels','on')

model.VacuumPermittivity = 8.8541878128E-12;
electromagneticProperties(model,"RelativePermittivity",78,"Conductivity",0.055)

% Boundary conditions for the system. Voltage may be changed to see the
% fields produced by applying different potentials.
bc1 = electromagneticBC(model,"Voltage",36,"Edge",1);
bc2 = electromagneticBC(model,"Voltage",0,"Edge",[2, 3, 5, 7, 8]);

% Generate a mesh with nodes for the solution to the partial differential equation to be fo
% Hmax defines the maximum element side length in the FEM model. A smaller
% value will produce a higher resolution solution but increase computation
% time.
generateMesh(model,"Hgrad",1.1,"Hmax",1e-8,'Hedge',{[2 3 5 7 8],1e-9},'Hvertex',{[3 7],1e-9


% Solve PDE and store solutions in the structur
R = solve(model);

%Calculate the magnitude of the electric field from it's components.
Efield = sqrt(R.ElectricField.x.^2 + R.ElectricField.y.^2);

% Set up equally spaced points to form a grid to interpret the solution for potential on.
% Equal spacing is a requirement for MATLAB to calculate the gradient.
xdist = 0.0000000015;
```

```
ydist = 0.000000001;
x = -0.0000003:xdist:0.0000003;
y = 0:ydist:0.0000004;
[X,Y] = meshgrid(x,y);

% Interpolating the electric field on the points and supplying the spacing
% to the gradient function. FX and FY are the components of the electric
% field gradient.
Eintrp = interpolateElectricField(R,X,Y);
EintrpMag = abs(Eintrp.Ex.^2 + Eintrp.Ey.^2);
EintrpMag2 = reshape(EintrpMag, length(x),length(y));
[FX, FY] = gradient(EintrpMag2,xdist,ydist);

% Plot electric field near a single nanohole
figure();
pdeplot(model,"XYData",Efield,"Contour","on")
hold on
oldcmap = colormap("jet");
title('Electric Field Around a Single Nanohole')

% Find magnitude of the electric field gradient
gradE = sqrt(FX.^2 + FY.^2);

% Plot electric field gradient around one nanohole
figure()
surf(X*1e9,Y*1e9,log10(gradE),'EdgeColor','None');
view(2);
colormap(jet);
xlabel('x (nm)','FontSize',20);
ylabel('y (nm)','FontSize',20);
axis([-300 300 50 350]);
c = colorbar;
c.Label.String = 'log(E)';
c.Label.Interpreter = 'latex';
c.TickLabelInterpreter = "latex";
set(gca,'TickLabelInterpreter','latex','FontSize',14);
title('Magnitude of the electric field gradient around one nanohole','FontSize',24);

% Factors to be used in the calculation of the dielectrophoretic force and
% torque
factor = pi*8.8541878128e-12*78*(50e-9)^3;
realpart = 0.950487203008953;
impart = -1.226164207221302e-04;

% Calculate the DEP force and torque. The factor comes from the other
% terms in the equation for the dielectrophoretic force, it is
% representative of 100nm diameter beads and water as the medium.
force = gradE * 2 * factor * realpart;
torque = EintrpMag2 * -4 * factor * impart;

% Format figure titles using latex
set(0,'defaulttextinterpreter','latex')
figure();
```

```
% Plot the dielectrophoretic force Around Nanohole
surf(X*1e9, Y*1e9, log10(torque),'EdgeColor','None');
view(2);
colormap("jet");
xlabel('x (nm)','FontSize',20);
ylabel('y (nm)','FontSize',20);
axis([-300 300 0 300]);
c = colorbar;
c.Label.String = 'log($|\overrightarrow{\tau}_{DEP}| (Nm)$)';
c.Label.Interpreter = 'latex';
c.TickLabelInterpreter = "latex";
set(gca,'TickLabelInterpreter','latex','FontSize',14);
title('Magnitude of the torque on a nanoparticle around one nanohole at 289 V','FontSize',2
```

APPENDIX B - ARRAY HOLDER SCHEMATIC

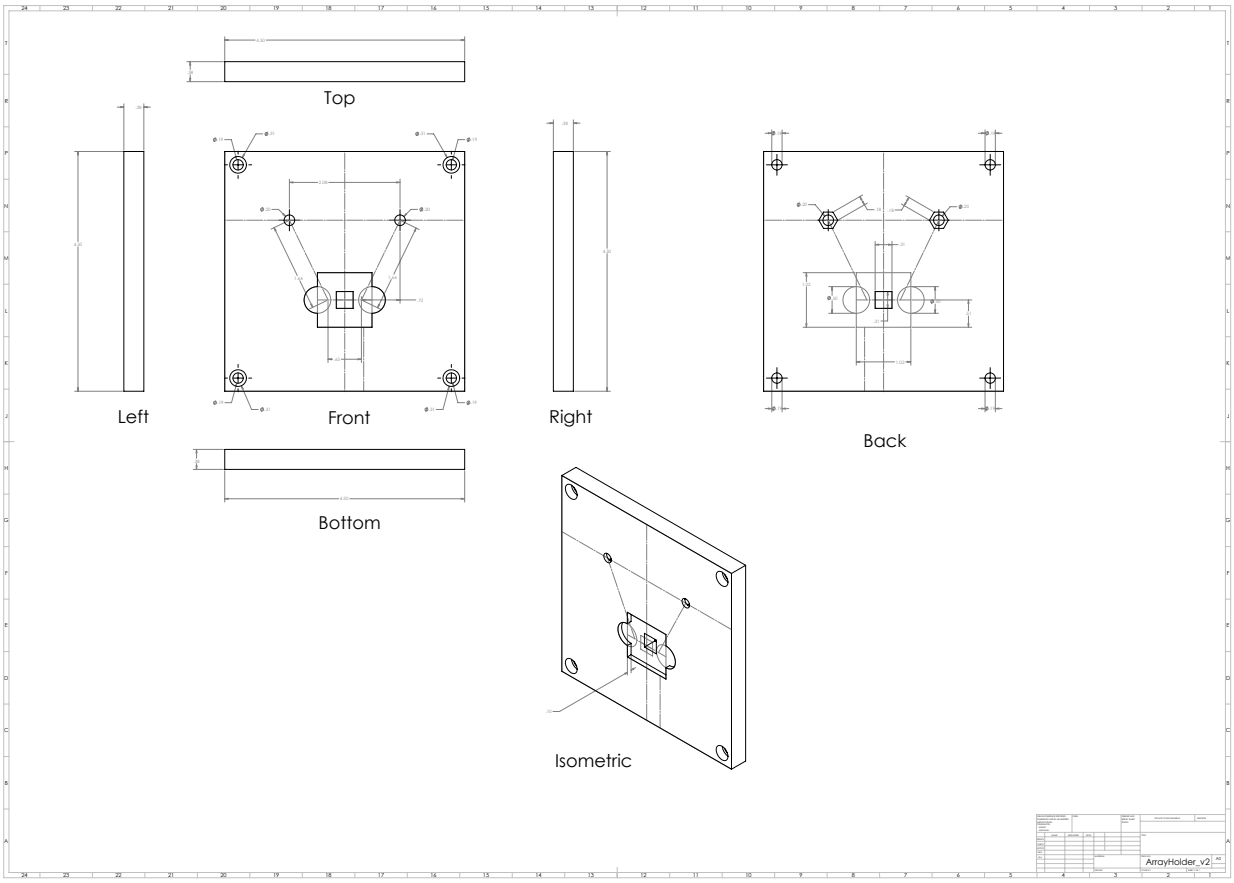

Figure B-1. Technical drawings for the array holder